

A Pneumatic Force Sensor for Enhanced Force Feedback in Robotic Colonoscopy

Korn Borvorntanajanya, *Graduate Student Member, IEEE*, Jialei Shi, Jabe F Ahmed,
Enrico Franco, and Ferdinando Rodriguez y Baena, *Member, IEEE*,

Abstract—Colonoscopy is often associated with significant discomfort, which can be mitigated by incorporating haptic feedback into robotic systems. This paper presents the design and experimental evaluation of a force sensing system integrated with haptic feedback for robotic colonoscopy. The system utilizes pneumatic sensing pouches mounted on the tip of a robotic colonoscope to capture contact forces in real-time and provide feedback to the operator via a haptic joystick. The pouch sensor demonstrates accuracy, with a maximum RMS error of 0.2 N during rigid phantom testing, while achieving 85% phase classification accuracy in detecting on-load and off-load states. Haptic force feedback significantly reduces peak interaction forces, lowering the maximum contact force from 1 N to 0.6 N without compromising task duration. Experiments in a soft colon phantom confirm the system's ability to detect forces in anatomically representative environments, demonstrating its potential for clinical use.

Index Terms—Pneumatic sensor, Soft growing robots, Minimally invasive surgery.

I. INTRODUCTION

ROBOTIC colonoscopy has the potential to significantly improve safety and reduce patient discomfort compared to traditional methods [1]. Among various robotic approaches, soft robotic systems powered by pneumatic actuation are particularly promising due to their inherent flexibility and safety when interacting with delicate tissues [2]. Early sensor-based continuum designs demonstrated semi-autonomous colonoscopy by combining real-time shape and force feedback to negotiate colonic folds with minimal operator input [3]. Subsequent pneumatic soft-robot prototypes for colonoscopy, such as the MorphGI system, use alternating anchoring and fluidic chambers to inchworm through colon phantoms with reduced mucosal stress [4]. The Soft Pneumatic Inchworm Double-balloon (SPID) robot employs two anchoring balloons and a 3-DoF central actuator for dexterous navigation in tortuous phantoms [5]. All of these designs still depend on cyclic pushing and pulling forces against

This work has been supported by the Engineering and Physical Sciences Research Council, Grant EP/X033546/1, and partially by the InnoHK initiative of the Innovation and Technology Commission of the Hong Kong Special Administrative Region Government. (*Corresponding author: Ferdinando Rodriguez y Baena*)

Korn Borvorntanajanya, Jialei Shi, Enrico Franco, and Ferdinando Rodriguez y Baena are with The Hamlyn Centre for Robotic Surgery, Imperial College London, SW7 2AZ, London, United Kingdom (e-mail: k.borvorntanajanya22@imperial.ac.uk, j.shi@imperial.ac.uk, e.franco11@imperial.ac.uk, f.rodriguez@imperial.ac.uk).

Jabe F Ahmed is with Department of Surgery & Cancer, Imperial College London, SW7 2AZ, London, United Kingdom (e-mail: jabed.ahmed@imperial.ac.uk)

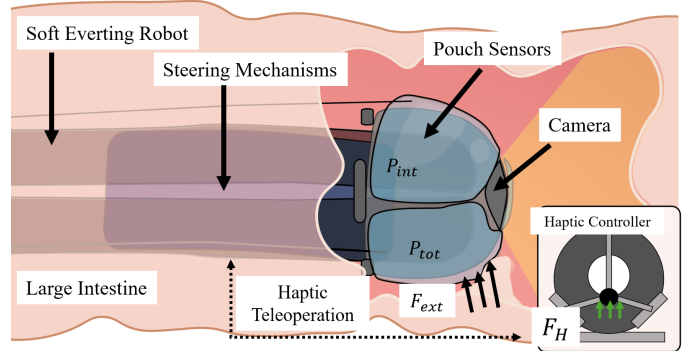


Fig. 1. An evertng robotic colonoscope integrated with pneumatic force sensors at the tip and haptic feedback system, detailing the key components and concepts.

the colon wall to advance. In contrast, soft growing robots offer unique advantages for navigating complex and confined environments, such as the human colon, as they can advance without relying on friction against surrounding structures [6]. This is achieved through an eversion mechanism, where a thin-walled tube lengthens by unfolding its inner layer when pressurized [7]. Soft growing robots have been successfully employed in diverse applications, including inspection, search-and-rescue operations, and minimally invasive surgery [8], [9].

Our long-term goal is to develop a soft robotic endoscope capable of navigating hollow visceral organs through eversion, aiming to reduce patient discomfort during colonoscopy procedures [10]. This approach allows for forward movement without the need for the user to apply a manual pushing motion, which is a common source of discomfort in traditional colonoscopy. By minimizing patient discomfort, we aim to increase participation rates in Bowel cancer screening programs, which often suffer from low uptake due to concerns about discomfort [11], [12].

However, while the evertng structure offers significant advantages, it introduces two critical challenges. First, there is an absence of haptic feedback in robotic colonoscopy [13], integrating haptic feedback into conventional colonoscopes has been shown to reduce peak push-pull forces [14]. Without real-time haptic feedback, operators have limited awareness of the forces exerted by the tip, increasing the risk of unintended tissue injury [15]. Second, the eversion mechanism concentrates forces primarily at the tip, with previous studies reporting tip forces up to 4 N [16] and 5 N [17], depending on the applied growth pressure and geometric dimensions of

the evert mechanism. Teleoperating evert robots and soft robots using a joystick have proven effective for basic navigation [18], [19], [20], but the absence of tactile feedback further limits the operator's ability to perceive and respond to interaction forces at the robot's tip. This challenge underscores the need for accurate estimation of contact forces and the integration of haptic feedback, which are essential for mitigating these risks, ensuring patient safety, and enhancing the usability of the robotic system [21], [22].

Various force-sensing techniques have been explored for use within the human body, including magnetic sensors, strain gauges, optical sensors, and pneumatic force sensors [23]. Piezoresistive sensing has also been implemented as a thin, flexible sleeve around the distal shaft of a conventional colonoscope, allowing real-time measurement of both radial and axial pressures exerted between the scope and a silicone phantom. While this approach can capture the full range of forces encountered during insertion and navigation, ensuring long-term electrical stability, bio-compatibility, and single-use sterility in clinical settings remains an open challenge that requires further development [24]. While magnetic and optical sensors offer advantages due to their non-contact working principles [25], magnetic sensors may not be compatible with colonoscopic environments that rely on electromagnetic navigation systems. Optical force sensors provide high precision across the forces encountered in colonoscopy [26]. When paired with glove-based haptic interfaces, these sensors can deliver insightful directional feedback and have been shown to reduce operator workload in studies [27]. Ongoing work on compact, low-power electronics aims to support disposable, sterile deployment. Additionally, because conventional colonoscopy involves forces distributed along the scope's shaft rather than concentrated solely at the tip, integrating tip-based feedback with distributed sensing or adaptive control strategies offers a promising path to more comprehensive force management during insertion.

Pneumatic force sensors, on the other hand, have emerged as a promising solution for force measurement in colonoscopy due to their broad sensing range, rapid response times, and purely mechanical operation [28], [29]. These sensors are ideal for sterile clinical environments, eliminating risks associated with electrical interference or contamination.

In our prior work, we proposed a pneumatic sensor [30] designed to measure in real-time the magnitude of forces acting at the tip of a conventional colonoscope. However, haptic feedback was not investigated. In addition, integrating the sensor with a soft growing robot presents new challenges, including accurately capturing three-dimensional tip forces in an uncertain environment, compensating for unintended tip rotations caused by material slippage during eversion, and reliably converting these force measurements into directional stiffness commands for effective haptic feedback.

This work presents a first investigation into employing a real-time tele-operation with haptic feedback on a soft evert colonoscope by integrating a three-axis pneumatic force sensor at its tip (see Fig. 1). In summary, the main contributions of this paper include:

- The development of pneumatic force sensing pouches

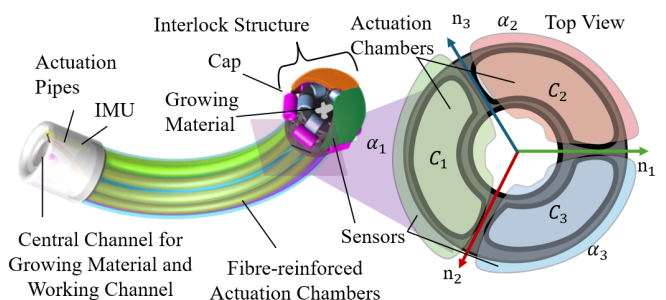


Fig. 2. Illustration of the steering mechanisms, IMU and pneumatic sensors on the cap of evert structure. $[C_1, C_2, C_3]$ represent the position of actuation chamber, and $[\alpha_1, \alpha_2, \alpha_3]$ denote the positions of pneumatic sensors on the cap.

tailored to an evert robot, which offers tip contact information of the robot during the operation.

- A new force-estimation algorithm that calculates three force magnitudes from the sensing pouches and robot states, such as steering angles, to determine contact force direction at the robot tip.
- The integration of the force sensor with a haptic joystick to provide real-time force feedback to the user during robotic colonoscopy.

II. MECHANICAL DESIGN AND ANALYSIS

This section presents the design analysis of the pneumatic force sensor that enables force feedback in the soft evert robot. The design of the pneumatic sensing pouch and of the evert robotic colonoscope prioritizes compatibility with the anatomical complexities of the human colon, which typically range from 2 to 4 cm in diameter [31]. In addition to anatomical fit, the system design considers clinically relevant contact forces. Human GI tissue studies indicate that contact forces above 10 N can pose a risk of tissue injury [32], while tissue deformation begins at approximately 1.5 N [33]. These thresholds were key considerations in ensuring safety during navigation.

A. Design of the Soft Evert Robot

The soft evert robot for colonoscopy considered in this work features an inflatable tubular structure that extends at its distal end through a process known as evert [7]. Evert robots involve applying pneumatic pressure between two layers of material, causing the inner layer to unfold at the robot's tip [34]. The growth only occurs at the tip, while the rest of the robot's body remains stationary relative to the colon wall. As such, contact forces between the robot and the colon are reduced. Our previous measurements indicate that contact forces along the robot's body during navigation range between approximately 0.13 and 0.57 N [35]. Consequently, all contact forces occur at the tip, and the pouch sensors capture the full range of navigation forces without the need to sense along the structure.

The material of the soft evert structure is silicone-coated ripstop nylon fabric (1.1 oz Silnylon, Ripstop by

the Roll), selected for its high flexibility and dual-layer silicone/polyurethane coating, which enhances durability and resistance to environmental factors. The fabrication process is adapted from the method described in [36]. In this work, the diameter of the tubular structure is 18 mm. This material is fed through a spool mechanism driven by a motor. To initiate growth, the base housing is pressurized, causing the fabric stored on the spool to unwind.

Steering is achieved through a custom-designed tip mechanism comprising a pneumatically actuated soft manipulator and an interlocking tip structure, as shown in Fig. 2(a). The actuation pipes for the steerable tip are deployed from another spool mechanism. The manipulator is fabricated from a compliant elastomer with nine actuation chambers arranged around a central lumen [37], through which the evertting material passes. For omni-directional steering, adjacent chambers are internally connected in groups of three (C_1, C_2, C_3), allowing the manipulator to bend in multiple directions [38]. To ensure that the manipulator remains at the advancing tip of the evertting structure, an interlocking mechanism with six sets of rollers is attached at the tip.

Due to the slippery nature of the nylon fabric and the design of the interlocking mechanism, the interlocking cap tends to twist about the roll axis when the material evert. This rotation consequently alters the orientation of the bending angle produced by the steering mechanism, resulting in instability of the robot's navigation. An IMU (BWT901B, WitMotion) is embedded at the base of the steering mechanism, as shown in Fig. 2, to measure its roll angle ζ in real time.

B. Design of the Pneumatic Sensing Pouch

The sensor is positioned at the evertting tip, the primary point of interaction with the intestinal walls. Accurate force estimation at this location is crucial to prevent tissue damage [32], [39]. The pneumatic sensing pouch is designed to capture forces at the tip of the evertting structure. The design builds upon our prior work [30], which investigated force sensing with a conventional colonoscope. The new design consists of a three-sensor array, which allows calculating the direction of the forces applied to the robotic colonoscope. To this end, three sensors ($\alpha_1, \alpha_2, \alpha_3$) are mounted on a hemispherical cap as shown in Fig. 2.

Each sensor has a design footprint as shown in Fig. 3(a), with one of the three areas of the cap (120 degree). It features a 2D line pattern that enhances force sensitivity and ensures improved force distribution. The 2D line pattern divides the sensing area into four equal pouches. The area of the i th pouch is given by $A_{\text{sector}_i} = \frac{\Theta_i}{360}\pi(R_i^2 - r_i^2)$, where Θ is the sector's angle (120° for the first sector and 40° for each of the remaining three), and r_i and R_i are the inner and outer radii, respectively. These weld lines also guide the pouch's inflation path, maintaining contact with the curved cap surface (see Fig. 3(b)). The cut patterns on the sensor anchor it to the hemispherical cap without creating folds, as illustrated in Fig. 3(c). The external forces exerted on the hemispherical cap cause the pouches to deform inducing a pressure change proportional to the magnitude of the applied force, as illustrated in Fig. 1. The

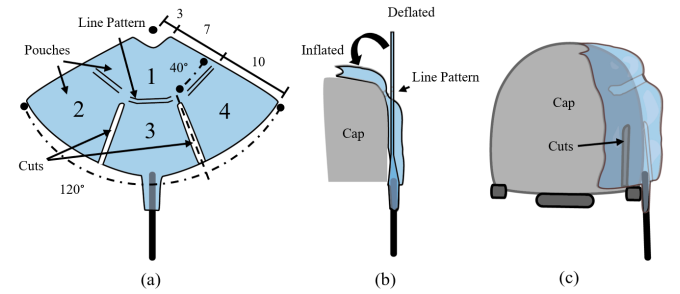


Fig. 3. Design of the pouch sensor and its mounting on the interlock cap. (a) Top-view schematic of the sensor arrangement. The numbers represent pouches on the sensor (b) Side views of the pouch in deflated and inflated states, demonstrating how inflation maintains conformal contact with the cap. (c) Cut patterns in the pouch material that secure it to the cap surface.

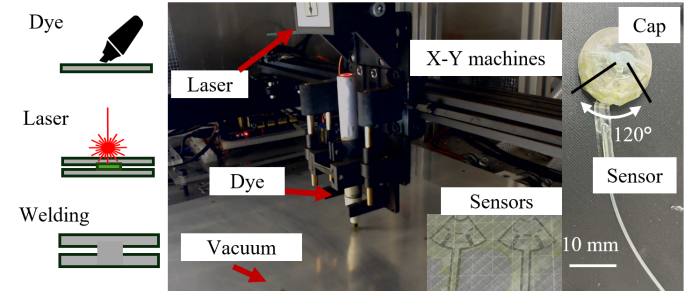


Fig. 4. Illustration of the sensing pouch fabrication process using laser welding, including an image of the laser welding machine, and integration of sensors onto the interlock cap.

sensing pouches are fabricated by laser welding two layers of flexible plastic sheets using a 2D laser welding machine from our track record [40]. Thus, the material used is biocompatible and suitable for single-use.

A 0.03 mm thick polyethylene sheet is placed on the vacuum plate of the welding machine. A solvent-based plastic welding material (Clearweld LD940B, Crysta-Lyn, USA) is applied to the sheet using a marker pen, see Fig. 4. Next, a second polyethylene sheet is positioned on top of the first layer with the assistance of vacuum suction. The laser melts and welds the two sheets together, creating sensing pouches with the required geometry. These pouches are subsequently cut and connected to a silicone tube (OD 1.4 mm in diameter and 150 cm in length) using PTFE tape (0.075 mm thick) and cyanoacrylate glue to ensure airtight seals. The sensing pouches are then mounted onto a 3D-printed cap using Vero-clear (Objet 400 printer).

III. SYSTEM CHARACTERIZATION

This section presents the experimental characterization of the force sensing system integrated with our soft evertting robot. In particular, we discuss the eversion force and the sensitivity of the sensing pouches.

A. Eversion Contact Force Characterization

Evertting robots utilize internal pneumatic pressure to progressively extend their outer tubing layer at the tip. Consequently, interaction forces primarily occur at the robot's tip, which is where an integrated force sensor should be located.

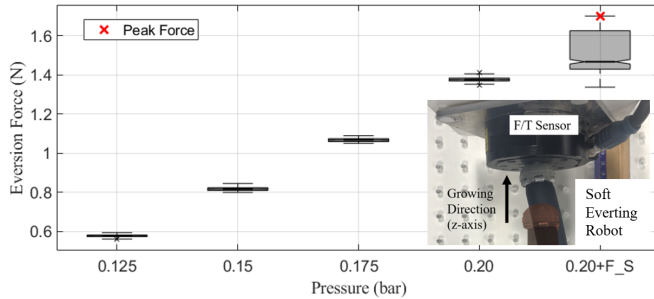


Fig. 5. Eversion force under different pressures applied to the evertng structure, with the tip steering manipulator actuated in the final step.

Experiments were conducted to assess the maximum eversion force during bending. To this end, the tip of the evertng robot was constrained by a force sensor (Gamma, ATI), while the tail was fixed to a stable base, as shown in Fig. 5. During each test, the growth pressure P_G increased from 0.125 bar to 0.20 bar in increments of 0.025 bar. Subsequently, steering was activated in random directions at the maximum growth pressure (0.2 bar), with pressures ranging from 0 to 3 bar applied to each actuated chamber of the steering manipulator. As shown in Fig. 5, the forces generated during growth ranged between $0.6 \sim 1.4 \pm (0.006 \sim 0.009)$ N as the growth pressure increased. When the bending force was included, the tip force slightly increased up to approximately 1.7 N. In our experiments, the maximum tip force of 1.7 N occurs when the tip contacts the environment perpendicularly, engaging all three pouch sensors simultaneously. To account for load sharing, we set each pouch's full-scale range at half this peak value (0.85 N).

B. Pneumatic Sensor Characterization

The external pressure P_{ext} caused by an external force F_{ext} is calculated as the difference between the total pressure P_{tot} and the initial pressure P_{int} , as described in [29], [30],

$$P_{\text{ext}} = P_{\text{tot}} - P_{\text{int}}. \quad (1)$$

Given the complex geometry of the pouch sensors, the relationship between P_{ext} and the applied force F_{ext} is modeled using the nonlinear function $H_{P_{\text{int}}}$, that is

$$F_{\text{ext}} = H_{P_{\text{int}}}(P_{\text{ext}}), \quad (2)$$

where $H_{P_{\text{int}}}$ was approximated using a fourth-order polynomial regression model derived from experimental data. This nonlinear model accounts for the geometric and material properties of the pouch sensors, enabling precise force estimation.

The experimental setup was designed to validate the sensor performance and characterize the relationship between force and pressure. A lead screw mechanism was employed to position a contact plate against the pouch sensors mounted on a cap attached to an Force/Torque (F/T) sensor (NANO 17, ATI), as illustrated in Fig. 6. The F/T sensor was incrementally moved along the z-axis in 0.1 mm steps, covering a total displacement of 2.0 mm from the initial position where changes in P_{tot} were observed. At each step, data was collected across 40 iterations

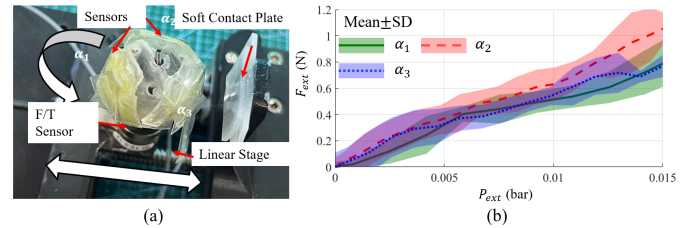


Fig. 6. Characteristic experiment of the external pressure and external force measured by three different pouch sensors. (a) is the characteristic setup, (b) Characteristic result.

using a 14-bit pressure sensor (4525DO, TE Connectivity), ensuring sufficient resolution and reliability. The experiments were repeated five times, with external forces ranging from 0 N to 1.2 N measured with a load cell, which served as the ground truth for F_{ext} . The initial pressure P_{int} was set to 0.155 bar for all trials, as shown in Fig. 6. Using the collected data, the $H_{P_{\text{int}}}$ model was derived, capturing the nonlinear behavior of the sensors under varying loads. Table I summarizes the coefficients of the fourth-order polynomial regression, which resulted in an RMSE of 0.09 N and an R^2 of 0.875. We selected a fourth-order polynomial for regression because it yielded the highest R^2 value compared to alternative models including second, third and fifth order.

TABLE I
POLYNOMIAL REGRESSION MODEL FOR $P_{\text{int}} = 0.155$ BAR

a_4	a_3	a_2	a_1	a_0
0.0079	-0.0037	-0.0546	0.2550	0.3229
$F_{\text{ext}} = a_4 P_{\text{ext}}^4 + a_3 P_{\text{ext}}^3 + a_2 P_{\text{ext}}^2 + a_1 P_{\text{ext}} + a_0$				

IV. SYSTEM INTEGRATION AND CONTROL STRATEGY

This section presents the overall framework for integrating the pneumatic pouch sensors with the robotic system and describes the control strategies employed to ensure effective operation. It begins by detailing the steering control strategy with haptic feedback, including the mapping of haptic device inputs to steering pressures and their application in bending actuation. Subsequently, the phase classification method is introduced to enable precise force estimation and dynamic state recognition during operation. Finally, the tip force vector calculation, derived from the steering information and the magnitude of force measured by the sensors, is discussed and extended to impedance control strategies, as shown in Fig. 7.

A. Steering Control Strategy with Haptic Feedback

1) Mapping Haptic Device Position to Steering Pressure:

The position input X_H of the haptic device (Omega 7, Force Dimension) forms a basis in \mathbb{R}^2 , representing motion in the x - and y -axes. This input is mapped to the steering pressures via a proportional gain K_p , expressed as:

$$P_S = \begin{bmatrix} P_x \\ P_y \end{bmatrix} = K_p(X_H - X_0), \quad (3)$$

where X_0 is the home position of the haptic device, P_S is the steering command input from users. P_x and P_y are the desired

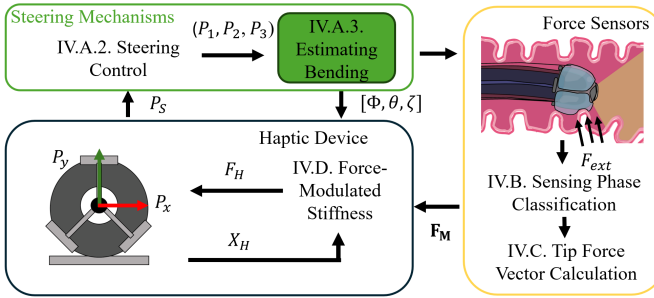


Fig. 7. System diagram depicting the integration of multiple sensors to measure force and direction, feeding data to the haptic device.

steering pressures along the x - and y -axes, respectively. This ensures that the input from the haptic device corresponds directly to planar steering control, enabling precise navigation within the two-dimensional input space of \mathbb{R}^2 .

2) *Steering Control with Pressure Mapping*: The steering manipulator exhibits two degrees of freedom in bending, characterized by the steering coordinates (θ, Φ) , where θ is the bending angle and Φ is the steering plane orientation (see Fig. 8). Actuation is achieved via three pressure chambers located at 120-degree intervals around the manipulator. The actuation pressures (P_1, P_2, P_3), govern the bending behavior of the manipulator. The relationship between the steering pressures and the actuation pressures is defined by a transformation matrix T , which incorporates twist compensation based on IMU data ζ , resulting in

$$\begin{bmatrix} P_x \\ P_y \end{bmatrix} = T \begin{bmatrix} P_1 \\ P_2 \\ P_3 \end{bmatrix}, T = \begin{bmatrix} \cos(\zeta) & -\sin(\zeta) \\ \sin(\zeta) & \cos(\zeta) \end{bmatrix} \begin{bmatrix} 0 & -\frac{1}{2} & \frac{\sqrt{3}}{2} \\ \frac{1}{2} & \frac{1}{2} & \frac{\sqrt{3}}{2} \end{bmatrix}. \quad (4)$$

Here, the 2×3 matrix encodes the geometric contributions of each chamber to planar bending: each column corresponds to a chamber positioned at 0° , 120° , and 240° around the manipulator. The entries $\{0, \frac{1}{2}, \frac{\sqrt{3}}{2}\}$ arise from the cosine and sine of these angles, mapping individual chamber pressures

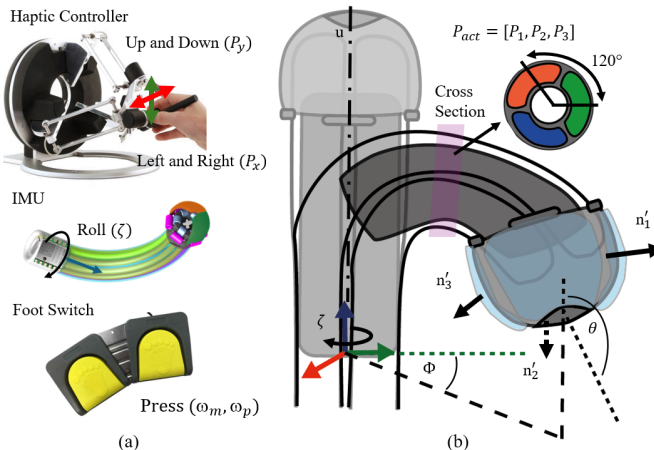


Fig. 8. (a) Tele-operation controller inputs with haptic feedback, including the haptic device, IMU, and foot switch; (b) Free-body diagram of the evertng robot.

into x and y components. The preceding 2×2 rotation matrix then compensates for any roll of the entire tip (measured by the IMU as ζ), ensuring that steering commands remain aligned with the intended bending plane despite twist. Thus P_1, P_2, P_3 are determined as

$$\begin{bmatrix} P_1 \\ P_2 \\ P_3 \end{bmatrix} = T^\dagger \begin{bmatrix} P_x \\ P_y \end{bmatrix}, \quad (5)$$

where T^\dagger is the pseudo-inverse of T . The pressures are then normalized and constrained between 0 bar and the maximum pressure $P_{\max} = 3$ bar as

$$P_i = \text{clip}(P_i, 0, P_{\max}), \quad i = 1, 2, 3. \quad (6)$$

The Supplementary Video further details this section.

3) *Estimating Bending Angles Φ and θ* : The bending angle θ and the steering orientation Φ are estimated based on the pressure vector P_S in (3) by using a model developed in prior work [35], that is

$$\theta = \sigma(\|P_S\|, P_G), \text{ and } \Phi = \text{arctan}2(P_y, P_x), \quad (7)$$

where $\|P_S\|$ is the magnitude of the steering pressure vector, P_G is the growth pressure set to static value at 0.20 bar in this work, $\sigma(\cdot, \cdot)$ is a mapping function, and $\text{arctan}2$ is the two-argument arctangent function that returns the angle in the correct quadrant.

4) *Foot switch controlled spool commands*: A foot switch actuates two motorized spools simultaneously: one for dispensing the evertng material and one for releasing the pneumatic tubing used by the steering mechanism. To achieve eversion, where the material must unfold at twice the tip's forward speed, the spools must satisfy the condition $r_m \omega_m = 2r_p \omega_p$, where r_m and ω_m are the radius and angular velocity of the material spool, and r_p and ω_p denote the radius and angular velocity of the pipe spool. When the foot switch is pressed, the material spool is driven at $\omega_m = 60$ RPM, yielding a tip growth speed of approximately 3.5 mm/s in free space.

B. Phase Classification of the Sensing Pouch

In this study, we propose a robust phase-classification method that converts raw pressure measurements into external force estimates in a system with dynamic refill states. The algorithm compensates for leakage in real time and classifies the system into five distinct operational phases: *No Load*, *Load Applied*, *Load Maintained*, *Load Removed*, and *Refill* as shown in Fig. 9. The classification depends on both the total pressure P_{tot} and its time derivative $\frac{dP}{dt}$, where dt is set to 0.02 seconds.

1) *No Load*: The *No Load* phase corresponds to the situation where no external force is applied. In this phase, P_{tot} remains equal to the initial pressure level, and $\frac{dP}{dt}$ remains below a predefined threshold τ .

2) *Load Applied*: The system enters the *Load Applied* phase when an external force is introduced, causing a rapid increase in P_{tot} . This phase is identified by monitoring $\frac{dP}{dt}$ for a positive rate of change exceeding τ .

3) *Load Maintained*: Once the load is applied and the pressure stabilizes, the system transitions to the *Load Maintained* phase. In this phase, P_{tot} remains relatively constant, and $\frac{dP}{dt}$ stays within a tolerance band indicating minimal fluctuation. However, P_{tot} in this phase is higher than the initial pressure P_{int} , resulting in a slight leakage. To ensure the accurate estimate of the external force applied to the sensor, the compensated pressure (see (9)) is calculated.

4) *Load Removed*: When the external force is removed, P_{tot} decreases noticeably, triggering the *Load Removed* phase. This transition is detected when $\frac{dP}{dt}$ is sufficiently negative (i.e., $\frac{dP}{dt} < -\tau$), indicating a release of pressure.

5) *Refill*: The system enters the *Refill* phase when $P_{\text{tot}} < P_{\text{int}} - \Delta P$, signifying the need to replenish the pouches. In summary,

$$P_{\text{tot}} = \begin{cases} P_{\text{int}} + P_{\text{ext}}, & \text{if } \frac{dP}{dt} \leq \tau \wedge P_{\text{tot}} \geq P_{\text{int}} - \Delta P \quad (\text{No Load}) \\ P_{\text{int}} + P_{\text{ext}}, & \text{if } \frac{dP}{dt} > \tau \quad (\text{Load Applied}, \ell = 1) \\ P_{\text{tot}}, & \text{if } \frac{dP}{dt} > -\tau \wedge \ell = 1 \quad (\text{Load Maintained}) \\ P_{\text{tot}} - P_{\text{ext}}, & \text{if } \frac{dP}{dt} < -\tau \wedge \ell = 1 \quad (\text{Load Removed}, \ell = 0) \\ P_{\text{int}}, & \text{if } P_{\text{tot}} < P_{\text{int}} - \Delta P \quad (\text{Refill}) \end{cases} \quad (8)$$

where τ is the threshold, and ℓ is a boolean variable indicating whether the load is applied (1 if true, 0 if false) as

$$\ell = \begin{cases} 1, & \text{if state} \in \{\text{Load Applied}, \text{Load Maintained}\}, \\ 0, & \text{otherwise.} \end{cases}$$

ΔP denotes the pressure difference caused by the operation of the non-return valve at the sensor inlet. This valve prevents backflow and enables the system to automatically replenishes the pouch under no-load conditions, compensating for leaks that arise due to the small gap at the connector interface. When total pressure exceeds the inlet pressure (load applied), this persistent small leak leads to a measurable pressure drop. When $\ell = 1$ (Load applied), a slight leakage at the sensor connectors is accounted for by compensating the total pressure based on the leakage rate over the load-applied interval. The compensated external pressure P_{comp} , derived from (2), is expressed as

$$P_{\text{comp}} = P_{\text{ext}} + \ell \cdot P_{\text{leak}}, \quad (9)$$

where

$$P_{\text{leak}} = \eta \cdot (t - t_{\ell}), \quad (10)$$

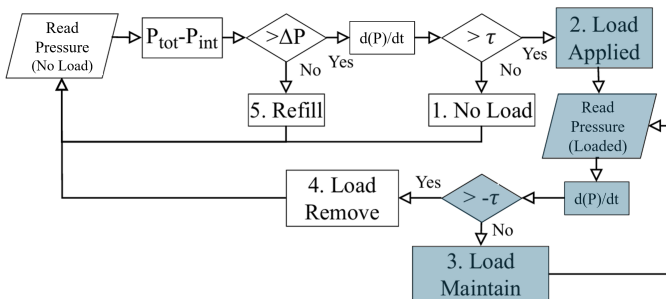


Fig. 9. Flowchart illustrating the classification of phases, including transitions between no load, load applied, load maintained, load remove, and refill states based on reading pressure. Blue color boxes represent when $\ell = 1$.

where η denotes leakage rate, that varies depending on the sensor and is determined experimentally during the initial calibration. t_{ℓ} is the time at which the load begins to be applied. The estimated external force F_{ext} is then computed as

$$F_{\text{ext}} = \ell \cdot H_{P_{\text{int}}}(P_{\text{comp}}), \quad (11)$$

where $H_{P_{\text{int}}}(\cdot)$ is given in (2).

C. Tip Force Vector Calculation

The bending information of the manipulator is captured through the bending plane angle Φ , the bending angle θ from (7) (see Fig. 8), and the sensor orientation in roll axis dynamically compensated with the IMU. Three force sensors are mounted on the interlock cap at angular positions $\alpha_1 = 0^\circ$, $\alpha_2 = 120^\circ$, and $\alpha_3 = 240^\circ$ relative to a reference direction, as illustrated in Fig. 2. However, since the interlock cap can rotate during eversion, the angular positions of the three sensors are dynamically compensated in real time using the angle ζ from the IMU sensor. When the manipulator is in its rest, straight configuration, the normal vectors of the sensors in the base frame are defined as

$$\mathbf{n}_i = \begin{bmatrix} \cos(\alpha_i + \zeta) \\ \sin(\alpha_i + \zeta) \\ 0 \end{bmatrix}, i = 1, 2, 3. \quad (12)$$

The manipulator bends by an angle θ about an axis that lies in the xy -plane at orientation Φ (and is therefore perpendicular to the global z -axis). The resulting rotation matrix $\mathbf{R} \in \mathbb{R}^{3 \times 3}$ is then computed using Rodrigues' rotation formula:

$$\mathbf{R} = \mathbf{I} + \sin \theta \mathbf{K} + (1 - \cos \theta) \mathbf{K}^2, \quad (13)$$

where \mathbf{K} is a skew-symmetric matrix based on the rotation axis, that is

$$\mathbf{K} = \begin{bmatrix} 0 & 0 & \cos(\Phi) \\ 0 & 0 & \sin(\Phi) \\ -\cos(\Phi) & -\sin(\Phi) & 0 \end{bmatrix}. \quad (14)$$

Here, the orientation angle Φ defines the bending plane, and the Pythagorean identity ensures the axis is normalized.

Each sensor i measures a scalar force magnitude F_{ext}^i . The force vector for each sensor, transformed to the base frame is denoted by $\mathbf{F}_{\text{ext}}^i = F_{\text{ext}}^i \mathbf{n}'_i$, $i = 1, 2, 3$, where \mathbf{n}'_i is the rotated normal vector of sensor i after bending, calculated as

$$\mathbf{n}'_i = \mathbf{R} \mathbf{n}_i = \begin{bmatrix} R_{11} \cos(\alpha_i + \zeta) + R_{12} \sin(\alpha_i + \zeta) \\ R_{21} \cos(\alpha_i + \zeta) + R_{22} \sin(\alpha_i + \zeta) \\ R_{31} \cos(\alpha_i + \zeta) + R_{32} \sin(\alpha_i + \zeta) \end{bmatrix}. \quad (15)$$

The total force vector at the manipulator's tip \mathbf{F}_M is the sum of the force vectors from all sensors according to (11) and (15), that is

$$\mathbf{F}_M = \sum_{i=1}^3 \mathbf{F}_{\text{ext}}^i = \sum_{i=1}^3 F_{\text{ext}}^i \mathbf{n}'_i. \quad (16)$$

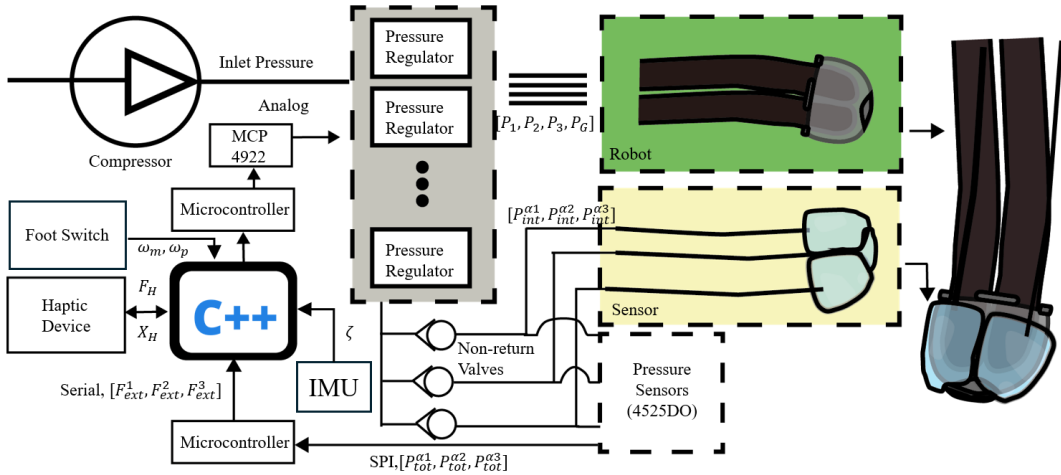


Fig. 10. System schematic of the pneumatic pouch sensor for robotic colonoscopy, illustrating the actuation architecture, force sensing units, and haptic device integration.

D. Impedance Control for Force-Modulated Stiffness

To provide force feedback to the operator, we modulate the stiffness of the haptic device at each discrete time step k to resist motion in the direction of the measured external force acting on the manipulator. This creates a sensation of increased resistance when the user attempts to move the haptic device handle in the direction of $\mathbf{F}_M(k)$ given in (16) as shown in Fig. 7. The force $F_H(k)$ rendered by the haptic device is

$$F_H(k) = \begin{cases} -K_{\text{stiff}} [X_H(k) - X_{F_M}(k)], & \|\mathbf{F}_M(k)\| \geq F_{\text{th}}, \\ 0, & \|\mathbf{F}_M(k)\| < F_{\text{th}}. \end{cases} \quad (17)$$

where K_{stiff} is the stiffness matrix, and $X_{F_M}(k)$ is reference position set when the external force exceeds a threshold, defined as

$$X_{F_M}(k) = \begin{cases} X_H(k), & \|\mathbf{F}_M(k)\| > F_{\text{th}} \wedge \|\mathbf{F}_M(k-1)\| \leq F_{\text{th}}, \\ X_{F_M}(k-1), & \text{otherwise}, \end{cases} \quad (18)$$

Then the stiffness vector K_{stiff} is defined as

$$K_{\text{stiff}} = K_0 + \lambda \|\mathbf{F}_M(k)\| dd^\top, \quad (19)$$

where, $d = \frac{\mathbf{F}_M(k)}{\|\mathbf{F}_M(k)\|}$ is the unit vector in the direction of external force, thus dd^\top acts as a projection matrix for any displacement ΔX_H , K_0 is the base stiffness, and λ denotes a scaling factor. This ensures that the increased stiffness is applied relative to the haptic device handle position at the moment when significant external force is detected.

V. EXPERIMENTAL EVALUATION

This section presents the experimental validation and evaluation of the haptic feedback control in robotic colonoscopy. Experiment 1 validates the accuracy of the force sensing system in a rigid phantom when teleoperated using a haptic joystick. Experiment 2 investigates the usability of the sensing system in a flexible environment during locomotion. Finally, Experiment 3 illustrates the effect of haptics on the forces generated by the operator in setups involving both soft and rigid phantoms.

A. Experimental Setup

Three pouch sensors are mounted on an interlock cap mechanism at the tip of the evertng structure as show in Fig. 10. The sensing pressures $P_{\text{tot}}^{[1,3]}$ were measured using a 14-bit digital sensor (4525DO, TE Connectivity) interfaced with a microcontroller (Arduino Rev4) via the SPI protocol. The evertng robot employed four proportional pneumatic valves (TeCNO Basic, Hoergiber) to regulate three pressure channels for steering and one channel for eversion. The valves are controlled through analog signals generated by DAC boards (MCP 4922, Microchip), which communicate with a microcontroller (NXP LPC1768, Mbed) using the SPI interface. All sensor data was collected using a C++ script via a serial link. An Omega 7 device (Force Dimension) was employed to drive eversion and steering while providing haptic feedback at a frequency of 50 Hz.

B. Force Sensing in a Rigid Phantom

1) *Protocol:* An initial pressure of 0.155 bar was set, corresponding to the polynomial regression ($H_{P_{\text{int}}}$) defined in Table I. The robot was driven inside a rigid phantom designed in an L-shape with a 90-degree bend, which was affixed to an F/Tsensor (Gamma ATI), see Fig. 11. The growth pressure

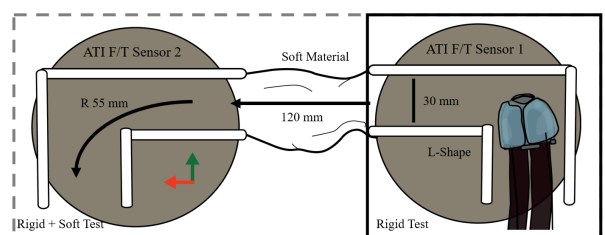


Fig. 11. Experimental setup for force measurements. Rigid phantom used in Experiment V.B., where two L-shaped segments are mounted on F/T sensors. Combined rigid-soft phantom for Experiment V.D., with the rigid L-shaped sections connected by a soft material segment to simulate varying tissue compliance.

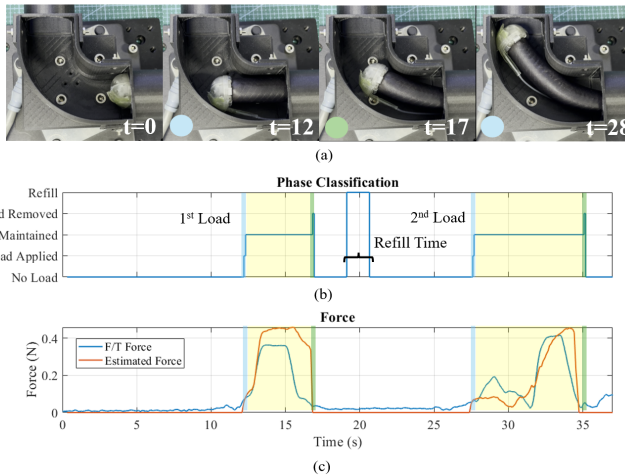


Fig. 12. Results for force sensing in a rigid phantom: (a) snapshots of the experiment showing two contact events with the rigid phantom; (b) phase classification based on the detected pressure; and (c) comparison between the estimated force (red line) and the ground-truth sensor measurements (note the gradual increase in robot weight over time).

True Phase	No Load	0	6	0		86.7 %
	Load Applied	6	30	4	0	
Load Maintained	6	4	30	0		75.0 %
Load Removed	6	0	0	34		
Refill				29		
	No Load	Load Applied	Load Maintained	Load Removed	Refill	Predicted Phase

Fig. 13. Confusion matrix for force sensing in a rigid phantom showing the phase classification results and % accuracy when running in a rigid phantom. This matrix compares the true phases with the predicted phases, that is *No Load*, *Load Applied*, *Load Maintained*, *Load Removed*, and *Refill* (see Section IV-B).

P_G was set to 0.2 bar. During the experiment, the robot made contact with the rigid phantom exclusively on the sensing pouch. The experiment was repeated five times to ensure consistency. The amplitude of the force was calculated as the root mean square of the forces along the x -y- and z -axes, that is, $F_{F/T} = \sqrt{F_x^2 + F_y^2 + F_z^2}$. The ground truth phase was recorded via video, synchronized with the time stamps of the recorded data as shown in Fig. 12(a). The Supplementary Video further reports details of this experiment.

2) *Result:* Fig. 12(b) shows that the maximum RMS error is approximately ± 0.2 N ($n = 5$). The maximum force generated by robot is around 0.6 N. Across five experiments, the robot made contact with the phantom a total of 40 times. The phase classification algorithm correctly inferred the phase (on-load or off-load) in 34 instances, achieving an accuracy of approximately 85%. During the on-load phase $\ell = 1$, the accuracy of detecting load maintenance decreased to around 75%. The system detected refill times in total 29 times over all experiments. However, as shown in Fig. 13, there is no ground truth for the refill time. The maximum refill time of the sensor during the experiments was approximately 2.4 seconds.

C. Force Feedback in a Silicone Phantom

1) *Protocol:* In this experiment, the robot was guided using a camera (OJH-15, EndoFun) mounted at the tip: the steering

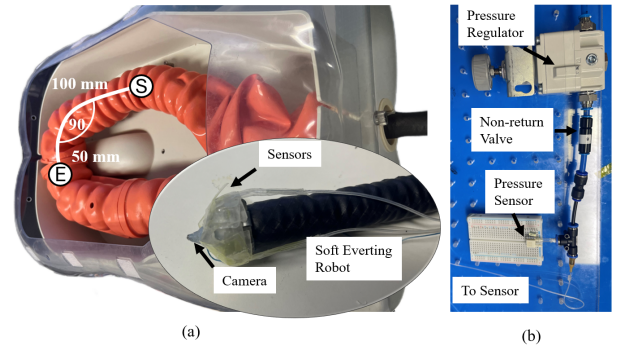


Fig. 14. Travel path on the soft silicone phantom (highlighted in white), and integration of the soft evertng robot with the force-sensor system and camera. (b) Sensing module for each pouch sensor, comprising a manual pressure regulator, non-return valve, and pressure sensor.

command was provided with the haptic device, while the eversion command was operated via a foot switch (FS1-P, Holso). The robot operated inside a colonoscopy training phantom (AK107, Adam Rouilly), see Fig. 14(a). The phantom was configured to simulate a pathway with both a straight section of 100 mm, a single turn of 90 degrees and a subsequent 50 mm straight section. The straight segment is intentionally offset from the lumen axis to mimic the common misalignment encountered at the start of a real procedure. This forces the operator to actively steer the tip into the correct trajectory, using both visual cues and haptic feedback, which results in occasional soft wall contacts that trigger the force sensor.

Two users, both experienced in operating the system with and without haptic feedback, were instructed to guide the robot from the starting point to the endpoint. The experiments were repeated three times. In the haptic feedback loop, the force threshold was set to $F_{\text{threshold}} = 0.1$ N, with $\lambda = 10$, and the maximum haptic force was constrained to $F_H = 3$ N. The forces and directions rendered from the tip sensors were

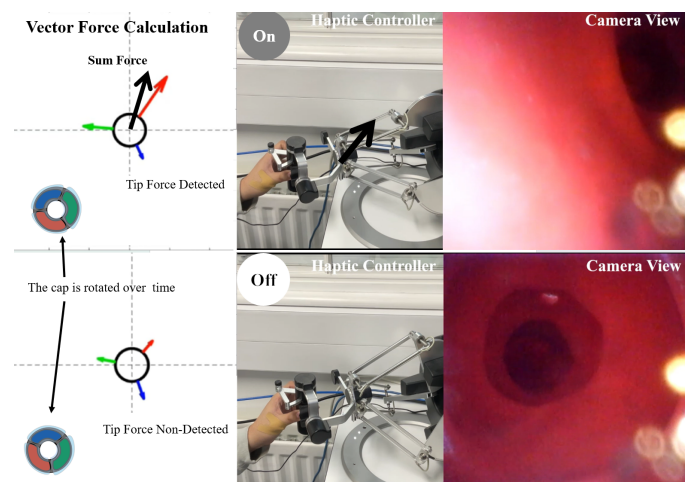


Fig. 15. Control interface with the haptic device during force sensing in a silicone phantom, illustrating the real-time calculation of the force vector from three pouch sensors during interaction with a soft environment (see Section IV-C). Top: haptic feedback activated. Bottom: haptic feedback deactivated (no external force). The corner inset shows a top-down view of the robot tip orientation corresponding to the eversion command.

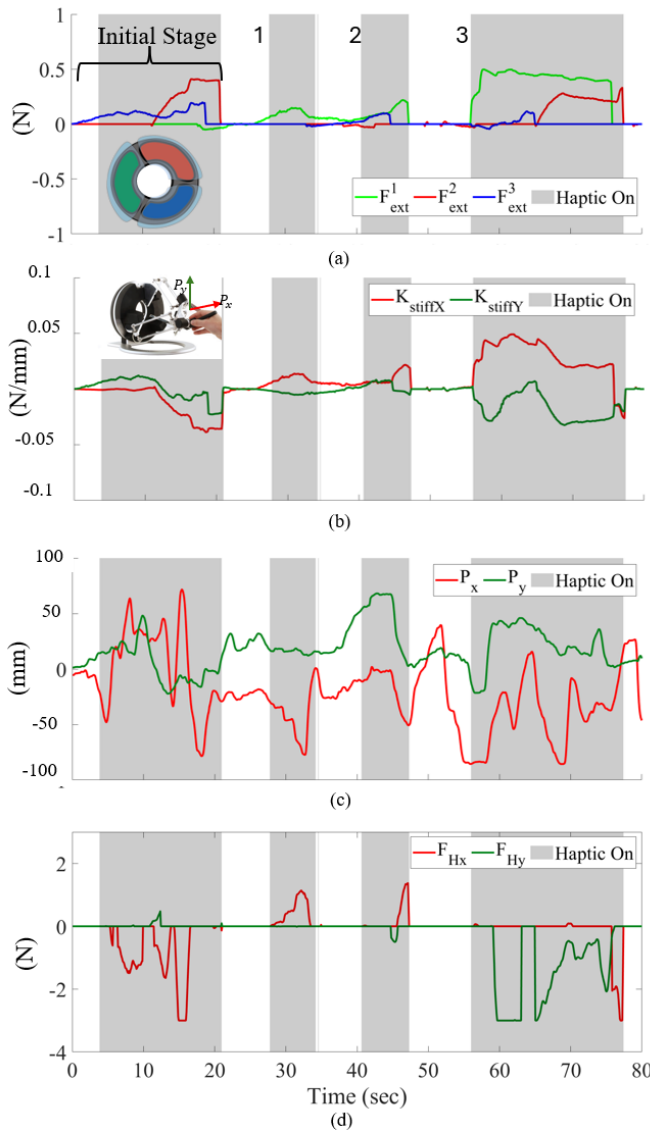


Fig. 16. Result of one of three trials in the soft phantom showing three contacts with the phantom wall during navigation: (a) Estimated forces from the three sensors (see Section IV-B), (b) stiffness vector calculated from the external force (see Section IV-D), (c) steering commands from the haptic device as in (IV-A1), and (d) force generated at the haptic handle based on stiffness and steering commands as in (17).

recorded over time and mapped alongside the position input of the haptic device, as shown in Fig. 15.

2) *Result:* Fig. 16(a) illustrates the forces detected by the sensors when the robot navigated through the soft phantom. The magnitudes from each sensor, combined with the steering information, were used to calculate the stiffness vector, as shown in Fig. 16(b). The user commands during the robot's navigation are plotted in Fig. 16(c), while the forces rendered at the haptic handle are presented in Fig. 16(d). During the first 20 seconds, which represent the initial stage, the user steered the robot to observe the direction. Throughout the test, the robot made contact with the phantom three times as the user attempted to steer the robot to the left ($P_x < 0$). In these instances, the left pouch sensor (green) successfully captured the external forces caused by the robot's motion,

corresponding to events 1, 2, and 3 (colored in gray) in Fig. 16. The external forces were detected until the steering command was set back to the initial position.

The maximum observed force, approximately 0.5 N, aligns with results from the rigid phantom study. Furthermore, Fig. 16(d) illustrates the forces generated at the haptic device when the robot's tip contacted the phantom, providing a clear correlation between contact forces and haptic feedback. Notably, the haptic feedback system attempts to push the handle back toward directions with no detected load, helping guide the operator to steer the robot away from contact areas.

D. Contact Force with and without Haptic Feedback

1) *Protocol:* Using image guidance from the endoscopic camera, two users navigated the robot through a third phantom consisting of both rigid and soft sections, see Fig. 17. The phantom was designed to replicate the anatomical trajectory of a human colon segment (e.g., rectum to sigmoid). The two rigid parts were equipped with F/T sensors to measure interaction forces. This setup enabled direct comparison of interaction forces across three conditions including haptic feedback on, haptic feedback off, and conventional colonoscopy, so that both peak and average forces could be quantified for each scenario. In the haptic feedback loop, $F_{\text{threshold}}$ was set to 0.2 N, and the maximum haptic force F_H was capped at 3 N. The force measured by the F/T sensors were recorded and compared between scenarios with and without haptic feedback. This experiment was repeated 8 times, including 4 times without haptic feedback and 4 times with haptic feedback. The Supplementary Video further details this experiment. Moreover, we performed three comparative trials using a conventional colonoscope along the same pathway, with a senior colonoscopist executing the procedure to benchmark performance against the evertting robot.

2) *Results:* Statistical analysis using a two-sample *t*-test reveals a significant difference in the maximum forces recorded with and without haptic feedback ($p < 0.01$). Specifically, the maximum force without haptic feedback was approximately 1 N, while haptic feedback reduced this value to around 0.6 N. This reduction in maximum force was observed consistently across both force sensors, as confirmed by individual statistical tests ($p < 0.01$) for each sensor position (Rectum and

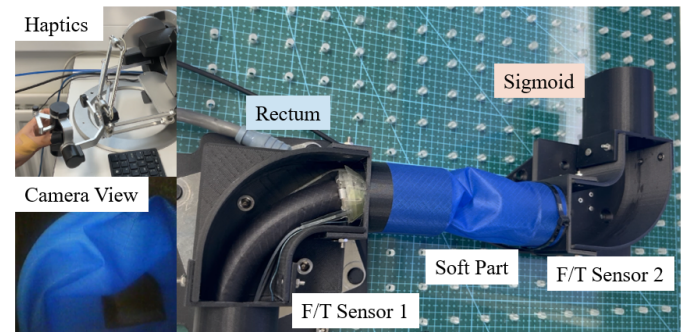


Fig. 17. Experiment setup for contact force interaction with the environment: Comparing interactions with and without haptic feedback.

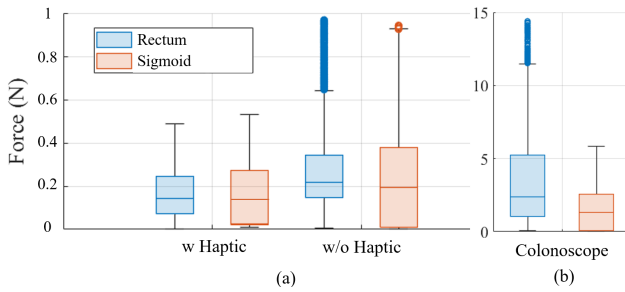


Fig. 18. Mean and standard deviation (SD) plot of the force applied on two force sensors (a) with and without haptic feedback across 8 trials, (b) conventional colonoscope across 3 trials.

Sigmoid). As shown in Fig. 18(a), the average force remained consistent at approximately 0.2 N, regardless of whether haptic feedback is used. Additionally, the time required to complete the task was slightly lower with haptic feedback (67 ± 10 seconds) compared to without haptic feedback (80 ± 20 seconds). In contrast, in three comparative trials using a conventional colonoscope, the maximum force at the rectum reached up to 15 N with a mean of approximately 3 N, while at the sigmoid it reached about 6.7 N with a mean around 1.8 N. The average completion time for these trials was around 32 seconds as shown in Fig. 18(b).

VI. DISCUSSION AND CONCLUSION

Pneumatic sensors were chosen for several key reasons: they offer a broad measurement range, and their response time enables real-time feedback at a rate of approximately 50 Hz. The purely mechanical design eliminates electrical components at the tip, avoiding interference risks and allowing the sensors to be fully disposable, eliminating the need for complex disinfection. Moreover, because both locomotion and sensing use the same compressed-air supply, valves, and control electronics, the system shares a unified air supply and control infrastructure, simplifying integration and easing maintenance.

The specifications of the proposed force sensing system, as determined from the characterization (Section II-B), are listed in Table II and compared to competitor solutions from the literature. The proposed sensor has similar footprint, rated force, and RMSE compared to [29]. The use of plastic sheets instead of silicone reduces unit-to-unit variability, meaning that the characteristic equation derived from a single calibration can be applied across multiple sensors with minimal error. This uniform behavior enhances consistency and reliability in multi-sensor setups, as shown in Fig. 6.

The first experiment demonstrated the ability of the sensing pouch to measure contact forces and classify phases during

interaction with a rigid phantom. The results showed a maximum RMS error of 0.2 N, indicating some limitations in detecting smaller force variations during operation. However, the RMS error of 0.09 N observed in the characterization test in Section III-B confirms that the sensor's accuracy at the tip is sufficient for estimating contact forces in most scenarios. The higher RMS error in this experiment was likely influenced by improper contact points between the sensor and the environment.

The phase classification algorithm achieved an accuracy of approximately 85% (34 correct classifications out of 40 contacts), successfully inferring the on-load and off-load states in most instances. However, the misclassification in six cases highlights room for improvement in the algorithm's reliability, particularly in scenarios with more complex or dynamic interactions. These misclassified cases occurred during the refill phase of the sensor, when it could not be activated by external forces. The maximum recorded refill time of approximately 2.4 seconds is noteworthy, as this downtime represents a period during which the sensor cannot detect any load. In the context of colonoscopy procedures, external forces may be applied to the system more frequently than this time interval, particularly during navigation through curved or constricted regions of the colon. Such scenarios require continuous and real-time force monitoring to ensure safe and effective operation. Prolonged refill times could therefore limit the sensor's responsiveness and compromise its ability to provide timely feedback during critical stages of the procedure. In future work, we will investigate machine learning approaches to enhance phase-classification reliability and reduce misclassifications, particularly during the refill phase.

In the second experiment, the sensors demonstrated their ability to detect forces in a flexible phantom environment, with maximum forces comparable to those observed in the rigid phantom experiment. This suggests the potential usability of the sensors in environments that mimic human anatomy. However, the absence of ground truth force measurements limits the quantitative assessment of the system's accuracy. Operators were able to successfully complete the standard navigation task in the phantom, showing that adding the sensor array and haptic feedback does not impede normal operation. The forces rendered on the haptic device aided operator control and navigation. This result highlights the importance of force feedback to enhance operator performance in dynamic clinical scenarios.

The final experimental results clearly demonstrate that integrating haptic feedback from tip sensor significantly enhances robotic navigation performance by effectively reducing peak interaction forces and improving operational efficiency. Specifically, the haptic feedback mechanism provides operators with critical tactile information whenever the robot encounters unseen obstacles, such as instances when the device becomes momentarily immobilized against phantom tissues outside the visual field of the camera. By guiding operators through directional stiffness cues and corresponding steering recommendations, the haptically enhanced system successfully lowered peak applied forces from approximately 1 N to just 0.6 N.

TABLE II
SPECIFICATIONS AND COMPARISONS OF POUCH SENSORS

Principle	Area (mm ²)	F_{\max} (N)	RMSE (%)
Fluid*	~104	0.85	10.6%
Fluid [29]	76 (expandable)	1.0	7.0%
Fluid [30]	285	9.6	3.5%

*This work.

For context, manual colonoscope insertions typically involve significantly higher interaction forces, with an average range between 2 N and 5 N, with occasional peaks surpassing 10 N, beyond which the risk of tissue perforation notably increases [32]. In comparison, our haptically augmented evertor robotic system consistently achieves peak contact forces of only 0.6 N, substantially below these critical thresholds and significantly lower than the robot's maximum tip force of 1.7 N, a level capable of deforming internal tissue [33]. This experiment (without Haptic feedback) was repeated by nine different colonoscopists using the same setup, and the results demonstrate a consistent trend. The maximum force applied by the evertor robot at the end of the rectum was 1.31 N (SD 0.14) and at the end of the sigmoid was 1.35 N (SD 0.18), whereas standard colonoscopy generated maximal forces of 19.03 N (SD 2.79) at the end of the rectum and 18.6 N (SD 1.38) at the end of the sigmoid [41]. This suggests that the proposed approach can result in safer interaction with the colon wall and can reduce patient discomfort.

Moreover, the average force during robotic navigation consistently remained around 0.2 N, indicating that the principal benefit of haptic feedback lies in its capability to mitigate transient peak forces without substantially affecting average interaction levels. Collectively, these findings emphasize the advantages of integrating haptic feedback for achieving safer, more controlled, and efficient robotic interaction with biological tissues.

Regarding operational efficiency, the haptically enhanced evertor robot required approximately 67 seconds to traverse a 200 mm segment. This duration represents a meaningful improvement over the 80 seconds observed in non-haptic operation, although it remains slower than conventional colonoscopes, which typically complete this distance in approximately 32 seconds. This performance difference arises from colonoscopists' greater familiarity and extensive practice with conventional devices compared to the robotic system. Nevertheless, given that standard clinical colonoscopies typically last around 25 minutes (i.e., to navigate the full 140–180 cm of the colon), the test duration with our haptic robot remains clinically appropriate. Therefore, despite being slower than a conventional colonoscope, the significant reduction in peak forces underscores the clinical potential of incorporating haptic feedback.

While the current soft–rigid phantom allowed precise quantification of haptic feedback, it does not replicate the compliance of real colon tissue. Future experiments will involve silicone phantoms instrumented with multiple force–torque sensors [4], enabling direct comparison between ground-truth contact forces and pouch sensor outputs under more realistic, tissue-like stiffness conditions.

Future work will focus on reducing the sensor's refill time by increasing the diameter of the supply pipes, enhancing its applicability in dynamic conditions characteristic of colonoscopy procedures. To integrate larger pipes, adjustments will be made to route them through the working channel of the evertor structure. Additionally, we plan to conduct phantom tests with a broader range of users, including both experts and non-experts. Based on users' comments and feedback, we

will continue to develop a dedicated haptic interface designed for our soft evertor robotic colonoscope. Finally, the current quantitative comparisons use phantom models that cannot fully replicate the biomechanical properties of the human colon. Future validation will involve ex-vivo tissue experiments to refine force measurements, followed by the development of anatomically accurate sensorized phantoms to prepare for clinical studies.

REFERENCES

- [1] H. K. Sekhon Inderjit Singh, E. R. Armstrong, S. Shah, and R. Mirnezami, "Application of robotic technologies in lower gastrointestinal tract endoscopy: A systematic review," *World Journal of Gastrointestinal Endoscopy*, vol. 13, no. 12, pp. 673–697, Dec. 2021.
- [2] L. Manfredi, "Endorobots for Colonoscopy: Design Challenges and Available Technologies," *Frontiers in Robotics and AI*, vol. 8, p. 209, July 2021.
- [3] G. Chen, M. T. Pham, and T. Redarce, "Sensor-based guidance control of a continuum robot for a semi-autonomous colonoscopy," *Robotics and Autonomous Systems*, vol. 57, pp. 712–722, June 2009.
- [4] J. E. Bernth, G. Zhang, D. Malas, G. Abrahams, B. Hayee, and H. Liu, "Morphgi: A self-propelling soft robotic endoscope through morphing shape," *Soft Robotics*, vol. 11, pp. 670–683, Aug. 2024.
- [5] L. Manfredi, E. Capoccia, G. Ciuti, and A. Cuschieri, "A soft pneumatic inchworm double balloon (spid) for colonoscopy," *Scientific Reports*, vol. 9, Dec. 2019.
- [6] E. W. Hawkes, L. H. Blumenschein, J. D. Greer, and A. M. Okamura, "A soft robot that navigates its environment through growth," *Science Robotics*, vol. 2, no. 8, p. 3028, July 2017.
- [7] J. D. Greer, T. K. Morimoto, A. M. Okamura, and E. W. Hawkes, "A Soft, Steerable Continuum Robot That Grows via Tip Extension," *Soft Robotics*, vol. 6, no. 1, pp. 95–108, Feb. 2019.
- [8] P. A. Der Maur, B. Djambazi, Y. Haberthur, P. Hormann, A. Kubler, M. Lustenberger, S. Sigrist, O. Vigen, J. Forster, F. Achermann, E. Hampp, R. K. Katzenbach, and R. Siegwart, "RoBoa: Construction and evaluation of a steerable vine robot for search and rescue applications," in *2021 IEEE 4th International Conference on Soft Robotics, RoboSoft*. IEEE, Apr. 2021.
- [9] P. Berthet-Rayne, S. M. Sadati, G. Petrou, N. Patel, S. Giannarou, D. R. Leff, and C. Bergeles, "Mammobot: A miniature steerable soft growing robot for early breast cancer detection," *IEEE Robotics and Automation Letters*, vol. 6, no. 3, pp. 5056–5063, July 2021.
- [10] I. Levy and I. M. Gralnek, "Complications of diagnostic colonoscopy, upper endoscopy, and enteroscopy," pp. 705–718, Oct. 2016.
- [11] D. A. Corley, C. D. Jensen, A. R. Marks, W. K. Zhao, J. K. Lee, C. A. Doubeni, A. G. Zauber, J. de Boer, B. H. Fireman, J. E. Schottinger, V. P. Quinn, N. R. Ghai, T. R. Levin, and C. P. Quesenberry, "Adenoma Detection Rate and Risk of Colorectal Cancer and Death," *New England Journal of Medicine*, vol. 370, no. 14, pp. 1298–1306, Apr. 2014.
- [12] S. Koo, L. J. Neilson, C. Von Wagner, and C. J. Rees, "The NHS bowel cancer screening program: Current perspectives on strategies for improvement," *Risk Management and Healthcare Policy*, vol. 10, pp. 177–187, Dec. 2017.
- [13] M. Bergholz, M. Ferle, and B. M. Weber, "The benefits of haptic feedback in robot assisted surgery and their moderators: a meta-analysis," *Scientific Reports*, vol. 13, Dec. 2023.
- [14] K. Kume, N. Sakai, and T. Goto, "Haptic feedback is useful in remote manipulation of flexible endoscopes," *Endoscopy International Open*, vol. 06, pp. E1134–E1139, Sep. 2018.
- [15] A. Talasaz and R. V. Patel, "Integration of force reflection with tactile sensing for minimally invasive robotics-assisted tumor localization," *IEEE Transactions on Haptics*, vol. 6, pp. 217–228, 2013.
- [16] F. Putzu, T. Abrar, and K. Althoefer, "Plant-inspired soft pneumatic eversion robot," in *2018 7th IEEE International Conference on Biomedical Robotics and Biomechatronics (Biorob)*, 2018, pp. 1327–1332.
- [17] S. G. Jeong, M. M. Coad, L. H. Blumenschein, M. Luo, U. Mehmood, J. H. Kim, A. M. Okamura, and J. H. Ryu, "A tip mount for transporting sensors and tools using soft growing robots," in *IEEE International Conference on Intelligent Robots and Systems*. Institute of Electrical and Electronics Engineers Inc., Oct. 2020, pp. 8781–8788.
- [18] F. Stroppa, M. Luo, K. Yoshida, M. M. Coad, L. H. Blumenschein, and A. M. Okamura, "Human interface for teleoperated object manipulation with a soft growing robot," in *2020 IEEE International Conference on Robotics and Automation (ICRA)*, 2020, pp. 726–732.

- [19] M. M. Coad, L. H. Blumenschein, S. Cutler, J. A. R. Zepeda, N. D. Naclerio, H. El-Hussieny, U. Mehmood, J.-H. Ryu, E. W. Hawkes, and A. M. Okamura, "Vine robots," *IEEE Robotics & Automation Magazine*, vol. 27, no. 3, pp. 120–132, 2020.
- [20] S. Treratanakulchai, E. Franco, and F. Rodriguez y Baena, "Model-free position control of a soft continuum manipulator in cartesian space," in *2023 International Conference on Control, Automation and Diagnosis (ICCAD)*, 2023, pp. 1–6.
- [21] A. M. Okamura, "Methods for haptic feedback in teleoperated robot-assisted surgery," *Ind. Robot: Int. J.*, vol. 31, pp. 499–508, Dec. 2004.
- [22] M. Bergholz, M. Ferle, and B. M. Weber, "The benefits of haptic feedback in robot assisted surgery and their moderators: A meta-analysis," *Sci. Rep.*, vol. 13, Dec. 2023.
- [23] H. Gao, X. Ai, Z. Sun, W. Chen, and A. Gao, "Progress in Force-Sensing Techniques for Surgical Robots," *Journal of Shanghai Jiaotong University (Science)*, vol. 28, no. 3, pp. 370–381, June 2023.
- [24] A. Vajpeyi, A. S. Naidu, N. A. Lavdas, J. D. E. Hawel, C. M. Schlachta, and R. V. Patel, "A novel, flexible, full-length, pressure-sensing sleeve for colonoscopes," *IEEE Sensors Journal*, vol. 24, no. 3, pp. 2513–2521, 2024.
- [25] T. P. Tomo, M. Regoli, A. Schmitz, L. Natale, H. Kristanto, S. Somlor, L. Jamone, G. Metta, and S. Sugano, "A New Silicone Structure for uSkin - A Soft, Distributed, Digital 3-Axis Skin Sensor and Its Integration on the Humanoid Robot iCub," *IEEE Robotics and Automation Letters*, vol. 3, no. 3, pp. 2584–2591, July 2018.
- [26] M. McCandless, A. Gerald, A. Carroll, H. Aihara, and S. Russo, "A soft robotic sleeve for safer colonoscopy procedures," *IEEE Robotics and Automation Letters*, vol. 6, no. 3, pp. 5292–5299, 2021.
- [27] A. Gerald, R. Battiwala, J. Ye, P. Hsu, H. Aihara, and S. Russo, "A Soft Robotic Haptic Feedback Glove for Colonoscopy Procedures," in *IEEE International Conference on Intelligent Robots and Systems*, vol. 2022-October. Institute of Electrical and Electronics Engineers Inc., 2022, pp. 583–590.
- [28] M. R. Mitchell, C. McFarland, and M. M. Coad, "Soft Air Pocket Force Sensors for Large Scale Flexible Robots," in *2023 IEEE International Conference on Soft Robotics, RoboSoft 2023*. Institute of Electrical and Electronics Engineers Inc., 2023.
- [29] L. Lindenroth, J. Merlin, S. Bano, J. G. Manjaly, N. Mehta, and D. Stoyanov, "Intrinsic Force Sensing for Motion Estimation in a Parallel, Fluidic Soft Robot for Endoluminal Interventions," *IEEE Robotics and Automation Letters*, vol. 7, no. 4, pp. 10 581–10 588, Oct. 2022.
- [30] K. Borvorntanajanya, J. F. Ahmed, M. Runciman, E. Franco, N. Patel, and F. R. y Baena, "Development of a low pressure pouch sensor for force measurement in colonoscopy procedures," in *2024 IEEE/RSJ International Conference on Intelligent Robots and Systems (IROS)*, 2024, pp. 2366–2372.
- [31] A. Alazmani, A. Hood, D. Jayne, A. Neville, and P. Culmer, "Quantitative assessment of colorectal morphology: Implications for robotic colonoscopy," *Medical Engineering and Physics*, vol. 38, pp. 148–154, Feb. 2016.
- [32] A. F. Khan, M. K. Macdonald, C. Streutker, C. Rowsell, J. Drake, and T. Grantcharov, "Tissue stress from laparoscopic grasper use and bowel injury in humans: Establishing intraoperative force boundaries," *BMJ Surgery, Interventions, and Health Technologies*, vol. 3, July 2021.
- [33] S. Johnson, M. Schultz, M. Scholze, T. Smith, J. Woodfield, and N. Hammer, "How much force is required to perforate a colon during colonoscopy? an experimental study," *Journal of the Mechanical Behavior of Biomedical Materials*, vol. 91, pp. 139–148, Mar. 2019.
- [34] K. Borvorntanajanya, S. Treratanakulchai, F. R. y. Rodriguez, and E. Franco, "Model-based tracking control of a soft growing robot for colonoscopy," *IEEE Transactions on Medical Robotics and Bionics*, vol. 6, no. 4, pp. 1354–1362, 2024.
- [35] J. Shi, K. Borvorntanajanya, K. Chen, E. Franco, and F. Rodriguez y Baena, "Design, control and evaluation of a novel soft evertng robot for colonoscopy," *IEEE Transactions on Robotics*, 2025.
- [36] N. D. Naclerio and E. W. Hawkes, "Simple, low-hysteresis, foldable, fabric pneumatic artificial muscle," *IEEE Trans. Robot. Autom.*, vol. 5, no. 2, pp. 3406–3413, 2020.
- [37] J. Shi, A. Sharifiati, S.-A. Abad, Y. Liu, J. S. Dai, and H. A. Wurdemann, "Stiffness modelling and analysis of soft fluidic-driven robots using lie theory," *The International Journal of Robotics Research*, vol. 43, no. 3, pp. 354–384, 2024.
- [38] J. Shi, S.-A. Abad, J. S. Dai, and H. A. Wurdemann, "Position and orientation control for hyperelastic multisegment continuum robots," *IEEE/ASME Transactions on Mechatronics*, vol. 29, no. 2, pp. 995–1006, 2024.
- [39] F. F. Leung, K. Borvorntanajanya, K. Chen, E. Zari, A. Garriga-Casanovas, E. Franco, F. R. y. Baena, P. Wai Yan Chiu, and Y. Yam, "Hybrid manipulator with force estimation for lower gastrointestinal interventions," *IEEE Robotics and Automation Letters*, vol. 9, no. 11, pp. 9709–9716, 2024.
- [40] M. Runciman, J. Avery, M. Zhao, A. Darzi, and G. P. Mylonas, "Deployable, Variable Stiffness, Cable Driven Robot for Minimally Invasive Surgery," *Frontiers in Robotics and AI*, vol. 6, Jan. 2020.
- [41] J. F. Ahmed, K. Borvorntanajanya, J. Shi, E. Franco, A. Darzi, F. R. Baena, and N. Patel, "Reducing applied force in colonoscopy using a novel soft robotic colonoscope: a head-to-head study," *Endoscopy International Open*, 6 2025.